

Theory of electron-phonon interactions in extended correlated systems probed by resonant inelastic x-ray scattering

Jinu Thomas^{1,2}, Debshikha Banerjee^{1,2}, Alberto Nocera^{3,4} and Steven Johnston^{1,2}

¹*Department of Physics and Astronomy, The University of Tennessee, Knoxville, Tennessee 37996, USA*

²*Institute for Advanced Materials and Manufacturing, University of Tennessee, Knoxville, Tennessee 37996, USA*

³*Stewart Blusson Quantum Matter Institute, University of British Columbia, Vancouver, British Columbia, Canada V6T 1Z4*

⁴*Department of Physics Astronomy, University of British Columbia, Vancouver, British Columbia, Canada V6T 1Z1*

(Dated: December 18, 2024)

An emerging application of resonant inelastic x-ray scattering (RIXS) is the study of lattice excitations and electron-phonon (e -ph) interactions in quantum materials. Despite the growing importance of this area of research, the community lacks a complete understanding of how the RIXS process excites the lattice and how these excitations encode information about the e -ph interactions. Here, we present a detailed study of the RIXS spectra of the Hubbard-Holstein model defined on extended one-dimensional lattices. Using the density matrix renormalization group (DMRG) method, we compute the RIXS response while treating the electron mobility, many-body interactions, and core-hole interactions on an equal footing. The predicted spectra exhibit notable differences from those obtained using the commonly adopted Lang-Firsov models, with important implications for analyzing past and future experiments. Our results provide a deeper understanding of how RIXS probes e -ph interactions and set the stage for a more realistic analysis of future experiments.

I. INTRODUCTION

Studying electron-phonon (e -ph) interactions in strongly correlated quantum materials is an exciting and rapidly emerging application of resonant inelastic x-ray scattering (RIXS) [1–3]. This advance has been enabled by significant improvements in instrument resolution, which have facilitated the observation of lattice excitations in diverse families of materials [4–22]. These efforts have been further bolstered by early theoretical models suggesting that the intensity of the lattice excitations provides direct information about the e -ph vertex $g(\mathbf{k}, \mathbf{q})$ [2, 23], as well as its coupling to the system’s electronic and magnetic parameters [6, 10]. However, all theoretical frameworks developed to date to describe these experiments approximate the system in some way, and the validity of each approach has yet to be checked rigorously. For this reason, the mechanics of how the lattice is excited during a RIXS experiment are not yet fully understood [1, 3].

Many of RIXS studies of the e -ph interaction [5, 12–14, 16] have relied on a single-site Lang-Firsov (SS-LF) framework [2] to analyze the data. This approach treats the infinite lattice in the atomic limit while coupling the local electron density to a single optical phonon branch. It neglects electron mobility and only allows for a \mathbf{q} -dependence via a \mathbf{q} -dependent e -ph coupling. Nevertheless, one can obtain an exact expression for the RIXS cross-section in this limit (see App. A) that captures some aspects of the experimental data. These include the generation of phonon excitations $I_n(\mathbf{q}) \equiv I(\mathbf{q}, \omega = n\Omega)$ at multiples of the phonon energy Ω , whose relative intensities grow in proportion to the e -ph coupling strength $|g(\mathbf{q})| \propto I_{n+1}(\mathbf{q})/I_n(\mathbf{q})$.

While the SS-LF-based models have been widely used to analyze experimental data, subsequent theoretical

studies have found that relaxing any of its assumptions can significantly affect the predicted spectra. For example, coupling to multiple modes in the atomic limit qualitatively changes the line shape and relative intensities of the phonon excitations [24]. Similarly, introducing electron mobility [25] and phonon dispersion [26] in the dilute limit leads to additional \mathbf{q} -dependence of the lattice excitations, even when the underlying e -ph coupling is momentum independent. The SS-LF-based models also fail to accurately capture potential coupling between the lattice and the core hole, which can affect the quantitative analysis of experiments [27] and lead to nontrivial renormalization of the core-hole potential once electron hopping processes are re-introduced [25]. These shortcomings highlight an urgent need for detailed modeling of e -ph coupling in RIXS on extended lattices.

Current approaches in this direction have neglected electron correlations [20, 23], focused on small clusters with only a small subset of relevant phonon modes [6, 10, 22], or have been restricted to the dilute limit [25, 26]. In contrast, the majority of RIXS studies in this space have been conducted on strongly correlated materials in or close to the half-filled Mott insulating regime. On the one hand, one might hope that the combination of strong Mott correlations and the core hole’s attractive potential will suppress the effects of electron mobility. On the other hand, magnetic and charge fluctuations will introduce new excitation pathways that can interfere with the lattice relaxation processes captured at the single-site level, as illustrated in Fig. 1. It is, therefore, unclear to what extent these effects will alter lattice excitations probed by RIXS and influence data analyses.

We address these open questions in this article by studying the RIXS spectra of the one-dimensional (1D) half-filled Hubbard-Holstein (HH) model. Using the numerically exact density matrix renormalization group (DMRG) method [28], we calculate the RIXS spectra

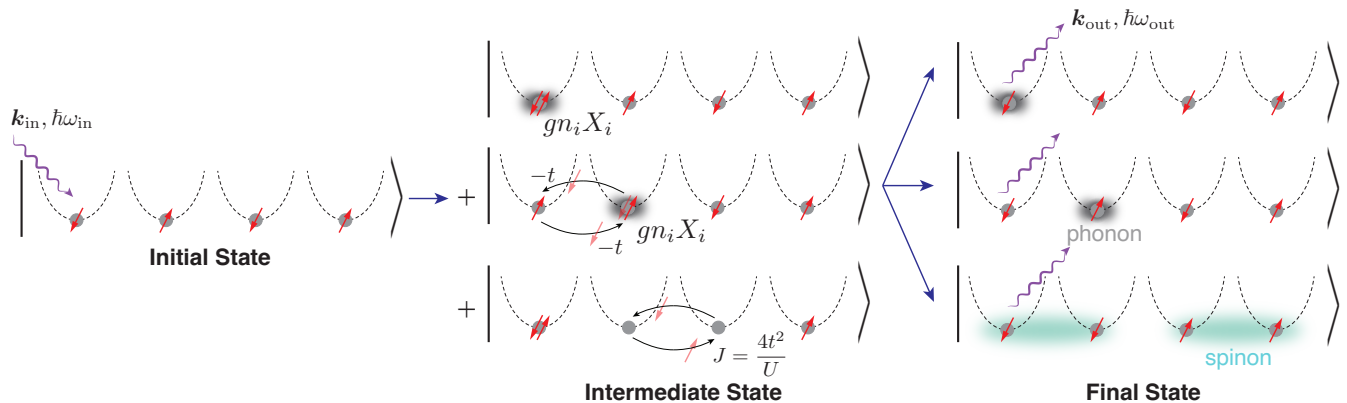


FIG. 1. Examples of different excitation pathways in RIXS measurements on a one-dimensional Mott insulator coupled to the lattice. The system's initial state consists of half-filled sites with strong antiferromagnetic correlations along the chain direction. After photon absorption, a core electron is promoted to the upper Hubbard band, creating a doubly occupied site (a doublon) that interacts with the system via hopping, e -ph coupling, and exchange processes. If hopping does not occur (top), the lattice can move in response to the doublon via the e -ph interaction, locally generating several phonon quanta before the core hole decays. Electron hopping opens additional excitation pathways that can interfere with this local process. For example, the doublon can delocalize to neighboring sites and create phonons before returning to the core-hole site and decaying (middle). This process produces low-energy phonon excitations on neighbor sites but requires more time than the process shown in the top row. Alternatively, double spin-flip processes can create two-spinon excitations, as sketched in the bottom row. The intermediate stages of these processes all interfere with one another during the RIXS process.

within the Kramers-Heisenberg (KH) formalism on extended chains while treating strong electron correlations, e -ph interactions, core-hole-lattice interactions, and any electron delocalization on an equal footing. We will demonstrate that each of these aspects can impact the spectra and should be considered in any quantitative analysis of an experiment. However, we also find that the strength of the core-hole potential plays a vital role in determining the relative importance of electron itinerancy. Our results thus contribute to the understanding of lattice excitations in RIXS and set the stage for more accurate analysis of experiments.

II. MODEL AND METHODS

A. The Hubbard-Holstein model

We consider the 1D HH Hamiltonian

$$\mathcal{H} = -t \sum_{j,\sigma} \left(\hat{c}_{j,\sigma}^\dagger \hat{c}_{j+1,\sigma} + \text{h.c.} \right) + U \sum_j \hat{n}_{j,\uparrow} \hat{n}_{j,\downarrow} + \Omega \sum_j \left(\hat{b}_j^\dagger \hat{b}_j + \frac{1}{2} \right) + g \sum_{j,\sigma} \hat{n}_{j,\sigma} (\hat{b}_j^\dagger + \hat{b}_j). \quad (1)$$

Here, $\hat{c}_{j,\sigma}^\dagger$ ($\hat{c}_{j,\sigma}$) creates (annihilates) an electron of spin σ at site j ; \hat{b}_j^\dagger (\hat{b}_j) creates (annihilates) phonon quanta at site j ; $\hat{n}_{j,\sigma} = \hat{c}_{j,\sigma}^\dagger \hat{c}_{j,\sigma}$ is the number operator; $t = 1$ is the nearest-neighbor hopping integral (and our unit of energy); U is the Hubbard interaction strength; Ω is the phonon energy ($\hbar = 1$), and g is the momentum-

independent e -ph interaction strength, which we take as positive without loss of generality.

The physics of the e -ph interaction is generally governed by two dimensionless parameters. The first is the dimensionless e -ph coupling $\lambda = g^2/2\Omega t$, which is equal to the ratio of the lattice deformation energy g^2/Ω to half the non-interacting bandwidth $W/2 = 2t$. The second is the adiabatic ratio Ω/E_F , which controls the degree of retardation in the model. Throughout this work, we focus on the half-filled model with $\frac{1}{L} \sum_{i,\sigma} \langle \hat{n}_{i,\sigma} \rangle = 1$ and $\Omega/t = 1$. This choice fixes $\Omega/E_F = 1/2$ and limits the size of the phonon's local Hilbert space needed for convergence while also retaining some degree of the retardation present in most materials [29, 30].

At half filling, the HH model has competing $\mathbf{q} = \pi/a$ charge density wave (CDW) and Mott insulating phases, with the latter dominating when $\lambda \lesssim U/W$ [31, 32]. The model also has a Luther-Emery liquid (LEL) phase for a region of small U/W and λ [33]. Throughout this work, we focus on $\lambda \leq 1/2$, where the model's ground state is a Mott insulator for most values of U/W ; however, we will also show results in the LEL phase, which appears for $U/W < 1$ for our parameters.

B. Formalism for the RIXS Calculations

We compute the RIXS spectra using the KH formalism, where the intensity is given by

$$I(\mathbf{q}, \omega) \propto \sum_f |F_{fi}(\mathbf{q})|^2 \delta(E_f - E_i - \omega) \quad (2)$$

with the scattering amplitude

$$F_{fi}(\mathbf{q}) = \sum_{\substack{n,j, \\ \sigma,\sigma'}} e^{i\mathbf{q}\cdot\mathbf{R}_j} \frac{\langle f|D_{j,\sigma'}^\dagger|n\rangle\langle n|D_{j,\sigma}|i\rangle}{E_i - E_n + \omega_{\text{in}} + i\Gamma/2}. \quad (3)$$

Here, $|i\rangle$, $|n\rangle$, and $|f\rangle$ are the initial, intermediate, and final states of the RIXS process, with energies E_i , E_n , and E_f , respectively; ω_{in} is the incident photon energy; $\Gamma/2$ is the inverse core-hole lifetime; ω is the energy difference between the incoming (ω_{in}) and outgoing (ω_{out}) photons; \mathbf{q} is the momentum transfer to the sample; $D_{j,\sigma}^\dagger$ and $D_{j,\sigma}$ are the local transition operators describing the core-valence transition on site j with spin σ ; and \mathbf{R}_j is the position of site j in the chain.

The single band HH model is most appropriate for modeling materials with a single hole in their active valence states, *e.g.*, Cu- L edge ($2p \rightarrow 3d$) measurements on cuprates. With this in mind, we treat the core-valence transition within the dipole approximation and parameterize $D_{j,\sigma} = M_{\epsilon,\sigma,\alpha} \hat{c}_{j,\sigma}^\dagger \hat{p}_{j,\alpha}$, where $\hat{p}_{j,\alpha}$ annihilates an electron in the α core level and $M_{\epsilon,\sigma,\alpha} = \langle 3d, \sigma | \hat{\epsilon} \cdot \hat{r} | 2p_\alpha \rangle$ is a polarization-dependent dipole matrix element. Throughout this work, we set $M_{\epsilon,\sigma,\alpha} = 1$ to focus on the lattice excitations rather than the polarization effects and assume that only a single core level is active in the scattering process. If there is a strong spin-orbit coupling (SOC) in the core orbitals, then α corresponds to the total angular momentum, and the electron spin is no longer a good quantum number [34]. In this case, the cross-section has contributions from spin conserving (SC) ($\sigma = \sigma'$) and non-spin conserving (NSC) ($\sigma \neq \sigma'$) channels. We will compute these contributions individually by appropriately restricting the spin summations appearing in Eq. (3). These two channels can be separated from one another in quasi-1D systems by analyzing the incoming and outgoing x-ray polarization [35].

When computing the intermediate states in Eq (3), we include the interaction between the core hole and valence electrons and a potential core-hole-lattice coupling. To capture these effects, local interactions of the form

$$\mathcal{H}_j^{\text{CH}} = V^{\text{CH}} \sum_{\sigma} \hat{n}_{j,\sigma} \hat{n}_j^{\text{CH}} + g_{\text{CH}} \hat{n}_j^{\text{CH}} (b_j^\dagger + b_j) \quad (4)$$

are added to Eq. (1), where $\hat{n}_j^{\text{CH}} = (1 - \hat{p}_{j,\alpha}^\dagger \hat{p}_{j,\alpha})$ is the number operator for the core level. Here, $V^{\text{CH}} < 0$ parameterizes the attractive potential between the core hole and valence electrons, and g_{CH} parameterizes the interaction between the core hole and the lattice (with a corresponding dimensionless coupling $\lambda_{\text{CH}} = g_{\text{CH}}^2/2\Omega t$). The intermediate state Hamiltonian with a core hole at site j is then $\mathcal{H}_j = \mathcal{H} + \mathcal{H}_j^{\text{CH}}$.

To obtain the resonant absorption edges for RIXS, we also compute the x-ray absorption spectra (XAS) using

Fermi's golden rule

$$\begin{aligned} I_{\text{XAS}}(\omega_{\text{in}}) &\propto \sum_n \left| \sum_{\sigma} \langle n | D_{j,\sigma} | i \rangle \right|^2 \delta(E_i - E_n + \omega_{\text{in}}) \\ &\propto -\text{Im} \sum_n \frac{|\sum_{\sigma} \langle n | D_{j,\sigma} | i \rangle|^2}{E_i - E_n + \omega_{\text{in}} + i\Gamma/2}. \end{aligned} \quad (5)$$

In the second line, we have followed the common practice of assuming that the inverse core-hole lifetime sets the energy broadening of the XAS spectra.

C. Computational Methods

We use DMRG [36, 37] to compute the RIXS and XAS spectra, as introduced in Ref. [28]. The approach is based on the Krylov space correction vector algorithm [38] and is briefly described in App. B. It computes the RIXS response without relying on any operator [39], core-hole-lifetime [40], or diagrammatic expansions [23, 41]. The only approximation that we introduce is the center-site approximation [42, 43] in Eqs. (B2) and (B6), which reduces the computational costs. We also use the Krylov space correction vector algorithm to compute the phonon spectral function $B(q, \omega)$ and dynamical charge $N(q, \omega)$ structure factors (see App. C).

We carried out all DMRG simulations using the DMRG++ code [44]. We typically kept $m = 500$ states and restricted the maximum number of phonon modes per site to $M = 10 - 17$ unless otherwise stated. Both values are chosen to ensure convergence of the ground state energy and XAS spectra (see also App. D). We fix the artificial broadening parameter $\eta = 0.2t$ for the RIXS calculations, which is consistent with the current experimental resolution assuming $t \approx 300$ meV.

III. RESULTS

We will now begin presenting our results, focusing first on the case without any core-hole-lattice coupling ($\lambda_{\text{CH}} = 0$). Sec. III E will present results with $\lambda_{\text{CH}} \neq 0$.

A. X-ray absorption spectroscopy

Figure 2a shows the XAS spectra as a function of e -ph coupling for the half-filled $L = 24$ site chains and fixed $U = 8t$, $V_c = -4t$, and $\Gamma/2 = t/4$. The system has a Mott insulating ground state for all values of λ shown in this panel. (Similar results for $V_c = -12t$ are shown in App. E.)

XAS spectra for the Hubbard model ($\lambda = 0$) have two resonances, which correspond to final states with different electron densities on the site where the core-hole is created [45]. The first is the so-called ‘‘well-screened’’ (WS) resonance, where the core electron is excited into

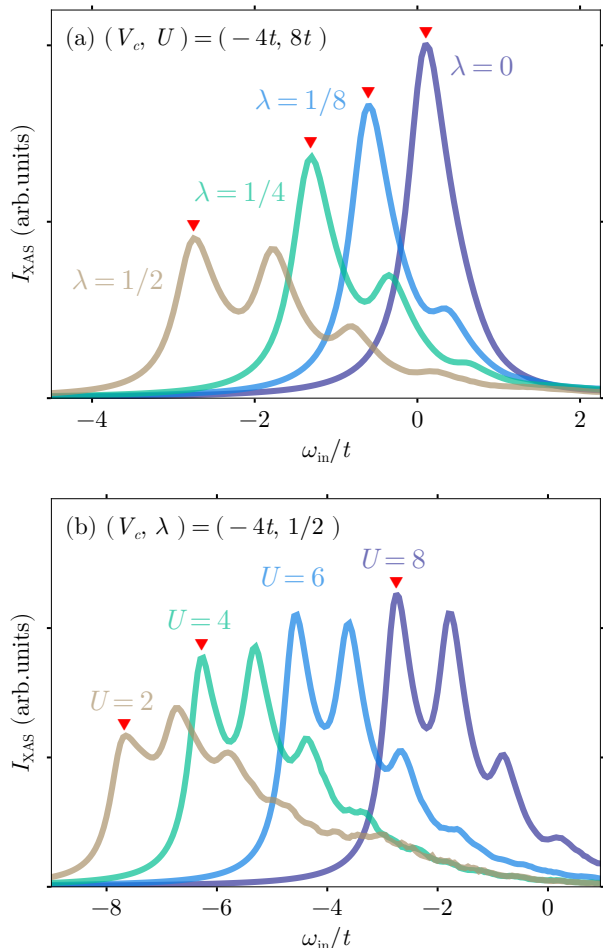


FIG. 2. (a) XAS as a function of the dimensionless e -ph coupling λ in a half-filled chain with $U = 8t$. Additional phonon harmonics are generated as λ increases. (b) XAS as a function of U for fixed $\lambda = 1/2$. Decreasing U shifts the XAS to lower energies and redistributes the weight among the phonon harmonics. In both panels, we fixed $L = 24$, $V_c = -4t$ and $\Gamma/2 = t/4$ and neglected the core-hole-lattice coupling ($\lambda_{\text{CH}} = 0$). The inverted red triangles indicate the incident energy used in subsequent RIXS calculations.

the valence orbital on the same site, creating a double occupation that screens the core-hole potential. The second is the “poor-screened” (PS) resonance, where the core electron is excited into a delocalized state, leaving the valence orbital of the core-hole site half-filled. In the limit $t \rightarrow 0$, these resonances appear at $E_{\text{WS}} \approx U + 2V_c$ and $E_{\text{PS}} \approx U + V_c$, respectively [45, 46]. The peak at $\omega_{\text{in}} = 0.1t$ in the $\lambda = 0$ spectra is the WS resonance.

Introducing the e -ph coupling shifts both resonances to lower energies and creates one or more phonon satellites at multiples of the phonon energy. The size of the shift can be estimated in the $t \rightarrow 0$ limit as $E_{\text{WS}} \approx U + 2V_c - 3\frac{q^2}{\Omega}$ and $E_{\text{PS}} \approx U + V_c - 3\frac{q^2}{\Omega}$, see Eq. (A2). Here, however, a non-zero hopping further shifts the res-

onance energies. The phonon satellites are analogous to the Franck-Condon broadening of the transition, which transfers spectral weight from the main resonance to the satellites as λ increases, producing an asymmetric line shape. As discussed later, this transfer also reduces the overall intensity of the RIXS spectra.

The results in Fig. 2a are qualitatively similar to those obtained from both the single-site [2, 24] and cluster-based treatments of the problem [6, 10]; however, we have observed subtle differences in terms of both the width and line shape of the individual phonon peaks (not shown). The importance of treating the extended system becomes much more apparent once we examine the U -dependence of the spectra for fixed λ , as shown in Fig. 2b. Varying U in the atomic limit only shifts the spectra on the ω_{in} axis. In contrast, decreasing U in the extended model shifts the main XAS resonance and changes the relative intensities of the phonon satellites. For example, for $U > 4t$, the intensity of the principal peak is larger than the first phonon harmonic, while this ratio is reversed for $U \leq 4t$. If these results are interpreted using a SS-LF framework, one would incorrectly conclude that the strength of the bare e -ph coupling increases as U decreases.

The spectra for $U = 2t$, which develops a noisy tail with a secondary peak at $\omega_{\text{in}} \approx -3t$, is particularly interesting. The model’s ground state is a LEL phase for this value of U , which we verified via the energy analysis described in Ref. [33]. In this case, we can resolve the WS and PS states at $\omega_{\text{in}} \approx -7.65t$ and $\approx -3.6t$, respectively, which are shifted $\approx 1.4t$ higher in energy relative to their locations in the atomic limit. We can also resolve two to three phonon satellites on the WS resonance before their intensity merges with the PS resonance. We have found that the PS resonance does not develop noticeable phonon satellites for all values of U and V_c we have checked (see App. E), which suggests that the itinerant PS final states are only weakly coupled to the lattice.

B. Resonant inelastic x-ray scattering

The low-energy RIXS spectra provide access to the system’s collective excitations [1]. The elementary magnetic excitations of the 1D Hubbard model are spinons, fractionalized spin-density waves that carry spin $S = 1/2$ and no charge [47]. Spinons must be created in pairs when excited by scattering probes, resulting in a multi-spinon continuum that has been observed in both inelastic neutron scattering (INS) [48–51] and RIXS experiments [35, 52, 53]. Four spinon excitations are also accessible in RIXS measurements, which appear in regions of phase space separated from the two-spinon continuum [53, 54]. 1D systems can also host fractionalized charge [55, 56] and orbital excitations [52]; however, these typically appear at high energies set by the Mott gap and crystal fields of the $3d$ orbitals, respectively [52, 57]. Thus, for large U/W , magnetic and lattice excitations dominate the low-energy RIXS spectra of systems like

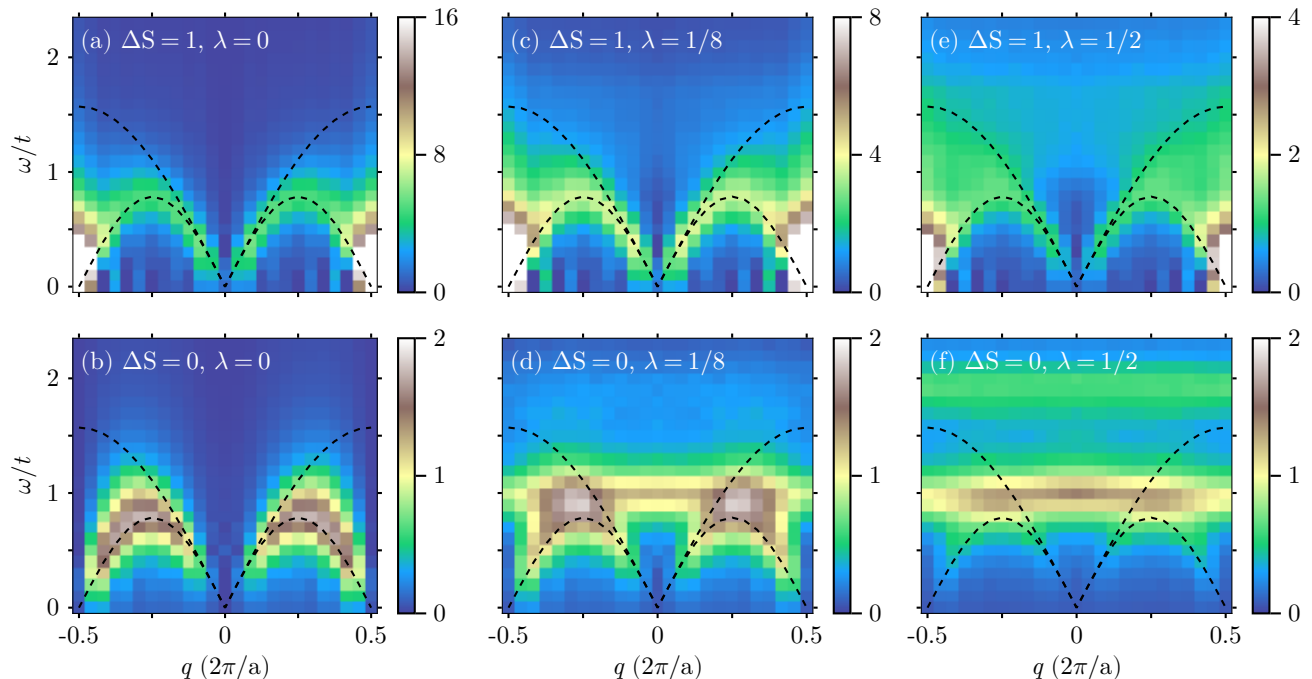


FIG. 3. The top and bottom rows show RIXS spectra in the non-spin conserving ($\Delta S = 1$) and spin conserving ($\Delta S = 0$) channels, respectively, for $\lambda = 0, 1/8$, and $1/2$, as indicated. The black dashed lines in each panel are the boundaries of the two-spinon continuum for the Hubbard model ($\lambda = 0$), assuming $J = 4t^2/U$. The intensity of the two-spinon continuum decreases in the NSC channel with increasing e -ph coupling without any change to the boundaries. The phonon excitations appear in the spin-conserving channel at multiples of the phonon frequency $\Omega = t$. All results were obtained on an $L = 24$ site chain with fixed $V_c = -4t$, $\Gamma/2 = t/4$, and $\lambda_{\text{CH}} = 0$. The incident photon energies are indicated by the inverted triangles in Fig. 2a.

the 1D cuprates and our model.

Figures 3a and 3b show the momentum-dependent RIXS spectra for our model in the NSC and SC channels, respectively. These were calculated on an $L = 24$ site chain with $U = 8t$ and $\lambda = \lambda_{\text{CH}} = 0$, $V_c = -4t$, $\Gamma/2 = t/4$, and with an incident energy tuned to the WS resonance, as indicated by the inverted red triangle in Fig. 2. The NSC magnetic excitations are, by definition, generated by direct spin-flip excitations, which are enabled by the large SOC in the core level [34, 58]. This scattering channel is analogous to spin-flip INS and thus resembles the two-spinon continuum observed in those experiments. The spectral weight in the RIXS spectra vanishes at zone-center $q = 0$ and is concentrated around the lower bound of the two-spinon continuum, consistent with the expectations for a Hubbard chain in the strong coupling limit [38, 59, 60]. In contrast, the SC magnetic excitations are generated via $\Delta S = 0$ double spin-flip processes like those shown in Fig. 1 [35, 60, 61]. The magnetic excitations in this channel thus resemble the dynamical spin-exchange correlation function [60, 62]. Notably, magnetic excitations in this channel are confined mainly to the two-spinon phase space and have vanishing spectral weight at $q = 0$ and $\pm\pi/a$ [60, 62].

Introducing the e -ph coupling generates phonon excitations in SC channel, whose intensity and number depend

on the strength of the interaction. For a weak coupling $\lambda = 1/8$ (Fig. 3d), the phonon excitation appears as a dispersionless feature that tracks the bare phonon energy across the entire Brillouin zone. The width of this feature in energy loss is set by the broadening parameter $\eta = 0.2t$. A second overtone (two-phonon excitation) appears at twice the phonon energy when the coupling is increased to $\lambda = 1/2$ (Fig. 3f).

Interestingly, a weak e -ph interaction does not alter the qualitative structure of the magnetic excitations [Figs. 3(c) & (d)] but it does change the relative intensities of the NSC and SC scattering channels. (Note the change in the intensity scales in Figs. 3c and 3e.) We attribute this reduction to the transfer of spectral weight from the main resonance to the phonon satellites observed in Fig. 2a, which we confirmed by comparing the ratio of the integrated spectral weight of the RIXS spectra to the ratio of the XAS peak intensities $I_{\text{xas}}(\omega_{\text{in}} + \Omega)/I_{\text{xas}}(\omega_{\text{in}})$. This observation has important implications for extracting quantum entanglement measures [1, 63–65] from the RIXS measurements of spin-1/2 systems like Sr_2CuO_3 , where phonon excitations have been observed [53] together with the two-spinon continuum. The e -ph coupling also alters the contrast between the two- and four-spinon excitations [54], which is most clearly seen in the $\lambda = 1/2$ spectra shown in Fig. 3e.

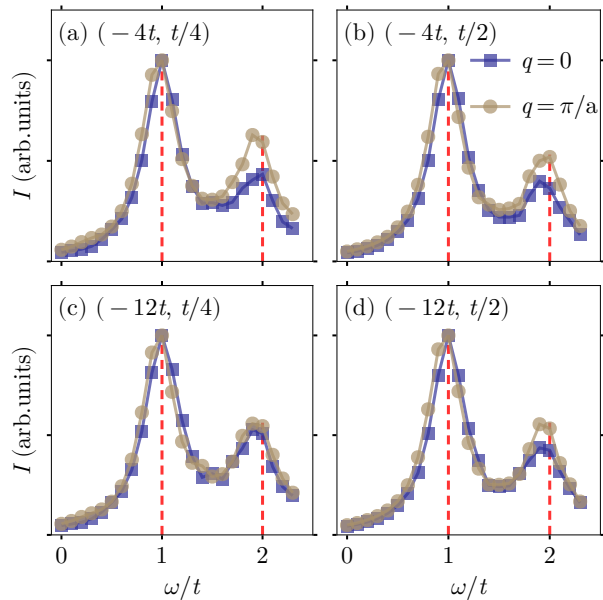


FIG. 4. RIXS spectra measured at the center ($q = 0$) and boundary ($q = \pi/a$) of the first Brillouin zone. Each panel shows results for different combinations of $(V_c, \Gamma/2)$, as indicated, while fixing $U = 8t$, $\Omega = t$, $\lambda = 1/2$, $\lambda_{\text{CH}} = 0$, and $L = 24$. Each spectrum is normalized to the intensity of the first phonon peak. All panels share the legend shown in panel (b). The red dashed lines indicate energy loss values $\omega = \Omega$ and $\omega = 2\Omega$. The SS-LF predicts no momentum dependence for all cases, while our calculations only observe this in (c).

Another important observation is how the boundaries of the two-spinon continuum remain unchanged when $g \neq 0$. In general, the e -ph coupling will mediate an effective, attractive interaction that reduces the effects of the on-site repulsion. In the anti-adiabatic limit ($\Omega \gg t$), the effective Hubbard interaction is $U_{\text{eff}} = U - \lambda W$. However, the e -ph interaction also dresses the hopping integrals with $t_{\text{eff}} = te^{-g^2/\Omega^2}$ in the strong coupling limit ($\lambda \gg 1$). While both effects should alter the effective exchange interaction $J = 4t^2/U$, they act in different directions. The spin excitations in our calculations remain within the two-spinon boundaries determined by the bare exchange interaction, suggesting that the renormalization of t and U , together with retardation effects, are conspiring to leave the effective exchange constant unrenormalized. (We have explicitly confirmed this observation also holds for the dynamical spin structure factor and, therefore, is unrelated to the RIXS cross-section.)

At first glance, the results shown in Fig. 3 are qualitatively consistent with the predictions of the SS-LF approach [2]. However, there are some important quantitative differences, particularly with respect to the momentum dependence of the phonon intensities. The first phonon excitation overlaps with the magnetic excitations for our choice of parameters. But we can exploit the vanishing weight of the SC magnetic excitations at $q = 0$ and π/a (see Fig. 3c) to isolate the contribu-

tions from the phonons at these momenta, as shown in Fig. 4. The SS-LF model predicts that the intensity of the phonon excitations is proportional to the momentum-resolved e -ph coupling $|g(q)|/\Gamma \propto I_2(q)/I_1(q)$, where $I_n(q) = I(q, \omega = n\Omega)$ is the intensity of the n th phonon excitation. For the Holstein model, one thus expects the ratio of these intensities to be constant in q . Our results, however, do not conform to this expectation.

Calculations in the dilute limit have shown that electron mobility introduces additional q -dependence in the intensity of the lattice excitations [25]. Our results show that this conclusion persists at finite carrier concentrations and deep into the strongly correlated Mott-insulating regime. For $V_c = -4t$, the ratio $I_2(q)/I_1(q)$ increases for $q = \pi/a$ relative to the value at $q = 0$ (See Fig. 4a). The bare e -ph coupling in our model is momentum-independent, and the renormalization of the phonon dispersion is negligible for these parameters (see also Fig. 6). Therefore, this momentum dependence must arise from the mobility of the electrons. This conclusion is also supported by the spectra's dependence on the strength of core-hole potential V_c and inverse core-hole lifetime $\Gamma/2$, which we discuss next.

C. Effects of the core-hole potential and lifetime

All transitions to the final states probed by RIXS occur via an intermediate state with a core hole and excited core electron. The nature of this intermediate state has two significant consequences for exciting the lattice. First, the inverse core-hole lifetime $\Gamma/2$ limits the time available to the lattice to respond to changes in density created in the intermediate state [2]. Second, the core-hole potential V_c controls the degree to which the excited electron can delocalize [25]. To explore these effects, Fig. 5 compares the RIXS spectra for fixed $\lambda = 1/2$, $\lambda_{\text{CH}} = 0$, and $U = 8t$ while varying V_c and $\Gamma/2$. In each case, we tune the incident photon energy to the first peak in the XAS spectra. For this discussion, we will use Fig. 5a (identical to Fig. 3f) as a reference spectrum with $V_c = -4t$ and $\Gamma/2 = t/4$. We then examine how changes in V_c and $\Gamma/2$ affect the spectra.

Halving the core-hole lifetime (doubling $\Gamma/2$) while keeping V_c fixed (Fig. 5b) reduces the overall intensity of the spectra. This change is more rapid for the two-spinon excitations (as evident from the difference plot), which almost vanish relative to the phonon excitations. We can rationalize this behavior by considering the relative time scales of the excitations measured against the core-hole lifetime. An intermediate state doublon induces an instantaneous change in the local lattice potential via a displacive mechanism, which will begin generating phonons immediately after it is created. Conversely, the SC magnetic excitations involve “slow” double spin-flip processes [35] and will be switched off if the core-hole lifetime is too short. We also find that the intensity of the two-phonon excitations decreases, consistent with the re-

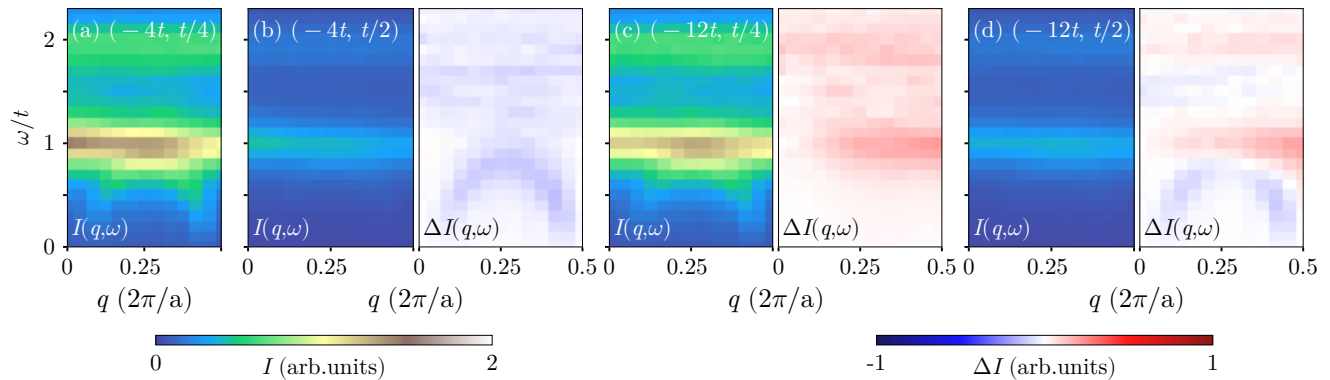


FIG. 5. RIXS spectra for $\lambda = 1/2$, $\lambda_{\text{CH}} = 0$, $U = 8t$, $L = 24$, and different values of $(V_c, \Gamma/2)$, as indicated. (a) shows the spectrum at $V_c = -4t$ and $\Gamma/2 = t/4$, which serves as our reference $I_{\text{ref}}(q, \omega)$. (b)-(d) RIXS spectra for various choices of V_c and $\Gamma/2$. The plot on the left of these panels is the calculated RIXS spectra $I(q, \omega)$ plotted over half of the first Brillouin zone $q = [0, \pi/a]$. The plot on the right of each panel is a difference spectrum $\Delta I(q, \omega) = I(q, \omega) - I_{\text{ref}}(q, \omega)$, which is obtained from subtracting the reference spectra shown in panel (a). When computing the difference plots, each spectrum was normalized to fix $I(q = 0, \omega = \Omega) = 1$ before taking the difference to focus on the relative (and sometimes subtle) changes in the magnetic and lattice intensities.

duced time for lattice relaxation. Notably, the differences in the relative phonon intensities $I_2(q)/I_1(q)$ at $q = 0$ and $q = \pi/a$ persist for $\Gamma/2 = t/2$ (see Fig. 4b), indicating that the electron itinerancy still contributes to the lattice excitations in this case.

Next, we increase the core-hole potential, which will tend to localize the intermediate state doublon. Setting $V_c = -12t$ while keeping $\Gamma/2 = t/4$, shown in Fig. 5c, redistributes the intensity of the phonons. We don't observe any significant changes in the spinon excitations here, while the intensity of the phonon excitations is enhanced relative to the spin contributions. This behavior is consistent with the picture that a more localized doublon can excite the lattice more effectively than it can induce double spin-flips. The intensity of phonon excitations also become more uniform in momentum space, which is consistent with the predictions of the SS-LF approach, indicating that $V_c = -12t$ is sufficient to localize the intermediate state doublon.

Finally, strengthening the core-hole potential and increasing the inverse core-hole lifetime combines these effects (Fig. 5d).

D. RIXS dependence on U

We now turn to weaker electronic correlations, which favors electron delocalization and allow competing CDW correlations to re-enter the problem. At half-filling, the charge correlations in the 1D HH model are strongest at $q = 2k_F = \pi/a$, which will soften the phonon dispersion at this wave vector. The charge fluctuations will also hybridize with the phonon modes near $q = 0$ if they extend low enough in energy [66]. To explore these effects, we report the SC RIXS spectra as a function of U in Fig. 6 for the same parameters used

in Fig. 5a. For reference, the second and third columns also show the corresponding phonon spectral functions $B(q, \omega)$ and dynamical charge structure factors $N(q, \omega)$, respectively.

The $U = 8t$ case [Fig. 6(a,d,g)] has a Mott-insulating ground state. In the previous sections, we discussed its RIXS spectra. The phonon spectral function closely tracks the bare phonon dispersion (Fig. 6d) and the charge excitations (Fig. 6g) are fully gapped. Reducing $U = 4t$ [Fig. 6(b,e,h)] narrows the Mott gap. The charge excitations (Fig. 6h) thus extend to lower energies where they begin to overlap and hybridize with the phonons. The phonons soften slightly near the zone boundary and develop a weak kink-like feature near $q = 0$ due to this hybridization. Similarly, $N(q, \omega)$ acquires a weak dispersionless feature resembling the renormalized phonon branch. The RIXS (Fig. 6b) spectra consist of overlapping contributions of the two-spinon, charge, and lattice excitations. In this case, the magnetic excitations extend to higher energies due to the increased exchange coupling $J = 4t^2/U$. The charge excitations also appear in the RIXS spectra as an arc of intensities above the magnetic excitations. The first phonon harmonic is easily resolved and tracks the renormalized phonon dispersion (indicated by the white dots). We also see indications of a weak second phonon harmonic; however, its intensity is reduced significantly, and it is much broader in energy—the latter results from the phonon dispersion, which widens the two-phonon phase space [26].

Reducing $U = 2t$ drives the system into a LEL ground state with significant CDW correlations. The charge excitations (Fig. 6i) extend even lower in energy and strongly hybridize with the phonons, producing a clear and sharp break in phonon dispersion at small q and Kohn anomaly at $q = \pi/a$. The magnetic excitations also extend to much higher energy. The first phonon ex-

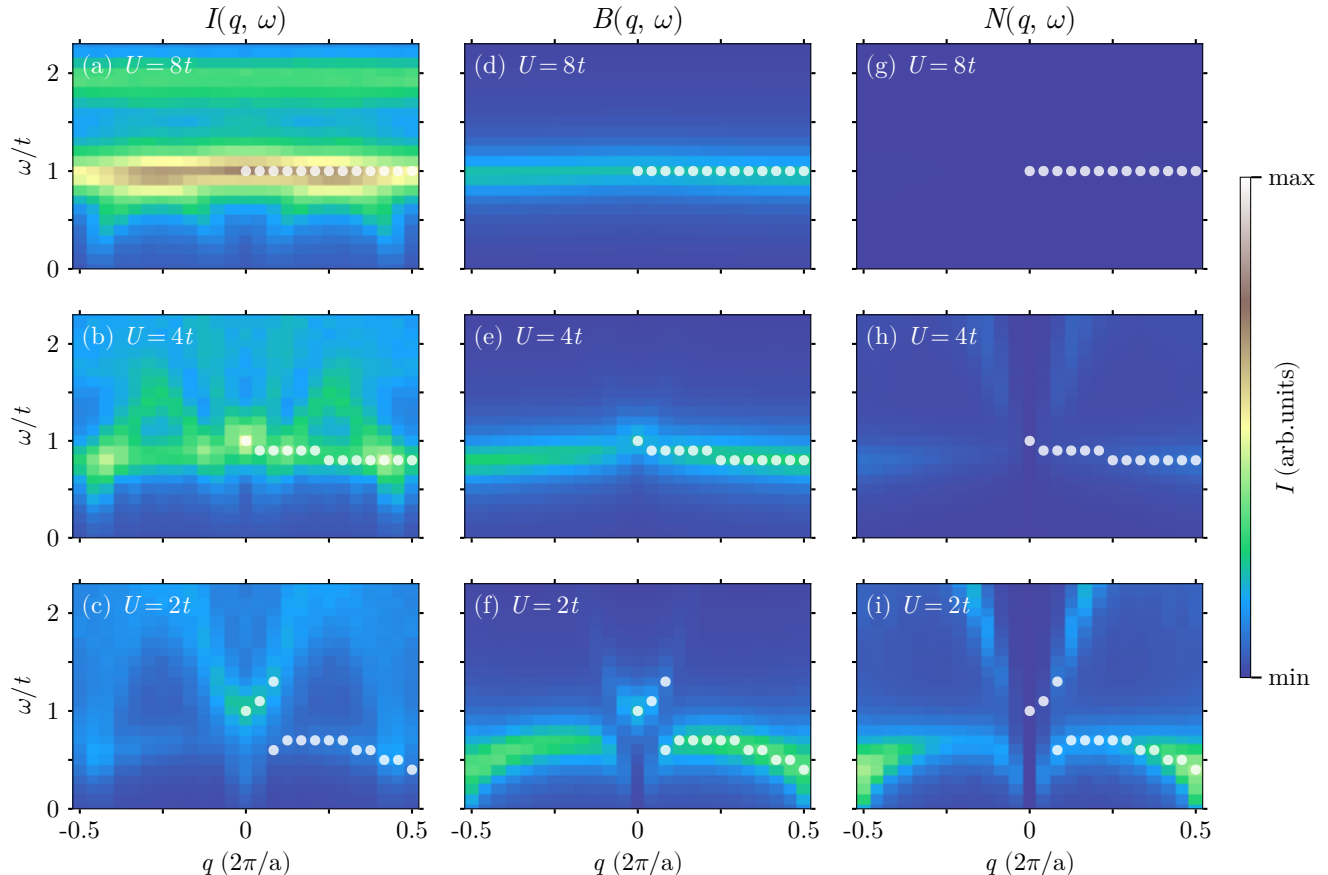


FIG. 6. (a)-(c) RIXS spectra in the SC channel as a function of U and fixed $\lambda = 1/2$, $\Omega = t$, $V_c = -4t$, $\Gamma/2 = t/4$, and $\lambda_{\text{CH}} = 0$. Panels (d)-(f) and (g)-(i) plot the corresponding phonon spectral functions $B(q, \omega)$ and dynamical charge structure factors $N(q, \omega)$, respectively. The top, middle, and bottom rows show results for $U = 8t$, $4t$, and $2t$, respectively. The white dots indicate the renormalized dispersion of the phonon, which was determined from the peak in the middle column. We obtained all results on $L = 24$ site chains. The RIXS spectra track the normalized phonon dispersion in all cases, including any hybridization effects with the charge excitations.

citation is extremely weak for this value of U , and we cannot resolve the second phonon harmonic.

The U -dependence of our results shows that the dispersion of the phonons observed in RIXS essentially tracks the renormalized dispersion, including any hybridization it may have with dispersive charge excitations. This result supports recent interpretations of the dispersive CDW excitations in two-dimensional cuprates [11, 15, 19]. The intensity of the phonon excitations also depends crucially on the degree of itinerancy in the system. The bare e -ph coupling used in Fig. 6 was fixed to $\lambda = 1/2$. Nevertheless, the intensity of the first and second phonon excitations decreases substantially as U decreases and develops a significant q -dependence, particularly for smaller values of U . These effects will significantly impact the interpretation of experiments. For example, based on these results, we expect that any mobility introduced by doping an insulating phase will decrease the intensity of the phonon excitations independent of any additional screening effects [67]. Therefore, the strength of

the e -ph coupling extracted from recent RIXS measurements on, for example, doped cuprates may be underestimated [13, 14, 21].

E. Core-hole-lattice coupling effects

Geondzhian and Gilmore [27] have recently argued that the core hole also couples to the lattice, leading to an effective exciton-lattice coupling in RIXS's intermediate state. If true, this would have important implications for interpreting experiments and extracting the magnitude of the valence band e -ph coupling from the data. In the SS-LF description, any core-hole-lattice interaction enters as an effective coupling $g_{\text{eff}} = g + g_{\text{CH}}$, which will enhance or suppress the phonon excitations depending on the relative sign of two coupling constants. However, the situation can be more complicated in an extended system. A core-hole-lattice coupling can promote or frustrate polaron formation at the core-hole site in the dilute limit,

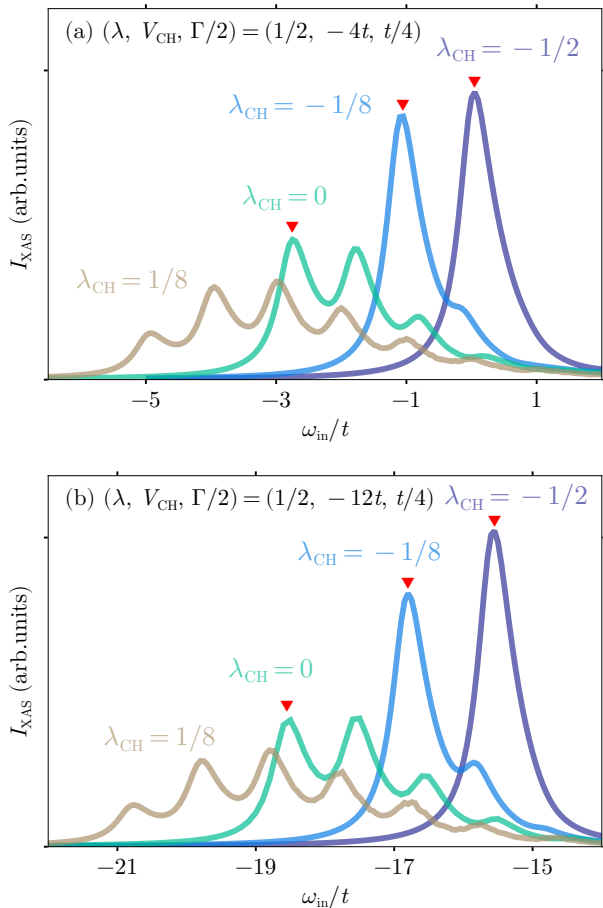


FIG. 7. XAS spectra for the Hubbard-Holstein model with an additional core-hole-lattice coupling λ_{CH} . Results were obtained for (a) $V_{\text{CH}} = -4t$ and (b) $V_{\text{CH}} = -12t$ while fixing $L = 24$, $U = 8t$, $\lambda = 1/2$, and $\Gamma/2 = t/4$. The inverted triangles indicate the incident photon energies of the RIXS calculations shown in Fig. 8. The XAS results qualitatively resemble the spectra for a local coupling of $g_{\text{eff}} = g + g_{\text{CH}}$.

renormalizing the effective core-hole potential [25]. The core-hole-lattice interaction can thus enhance or suppress mobility effects in the intermediate state, depending on its sign. However, whether this result holds at finite densities or in correlated systems like those considered here is unclear.

Motivated by this, we now examine these effects of setting $g_{\text{CH}} \neq 0$ [see Eq. (4)]. Our model assumes that the core-hole-lattice coupling is local and is only active in the intermediate state. First, we consider scenarios where the core-hole coupling either augments ($g_{\text{CH}}/g > 0$) or competes ($g_{\text{CH}}/g < 0$) with the local valence band coupling; however, the latter is expected if e -ph coupling arises from an electrostatic interaction between the charge density and atomic positions. [If an electron in the valence band decreases the lattice displacement ($g > 0$), then a core hole should increase it ($g_{\text{CH}} < 0$).] As the dimensionless coupling constant λ_{CH} is positive by definition,

we will append the sign of g_{CH} to distinguish the two scenarios [i.e., $\pm\lambda_{\text{CH}}$ for $g_{\text{CH}}/g > 0$ ($g_{\text{CH}}/g < 0$)].

Figure 7 shows XAS results as a function of λ_{CH} for fixed $\lambda = 1/2$, $U = 8t$, and $\Gamma/2 = t/4$. The additional core-hole coupling shifts the WS resonance. It redistributes the spectral weight of the phonon satellites in a way that is qualitatively consistent with the $g_{\text{eff}} \approx g + g_{\text{CH}}$ picture. However, we have observed quantitative and subtle qualitative differences when we compared the results shown here to spectra with an equivalent value of $g = g_{\text{eff}}$ and $g_{\text{CH}} = 0$ (not shown). These differences occur because g_{CH} only acts at the core-hole site and thus only affects local phonon creation while $t \neq 0$ opens up pathways for creating phonons at neighboring sites that do not couple to the core-hole.

Figure 8 shows the corresponding RIXS spectra. As mentioned, we expect $g_{\text{CH}}/g < 0$ for any coupling arising from electrostatic interactions, so we focus on this regime. For a shallow potential $V_c = -4t$ and a weak core-hole-lattice coupling $\lambda_{\text{CH}} = -1/8$ (Fig. 8b), the spectra resemble the $\lambda = 1/8$ case in Fig 3d. The second phonon harmonic is suppressed as the local effective coupling g_{eff} is reduced; however, the momentum-dependence of this feature becomes much more pronounced with $I(q = \pi/a, \omega = \Omega) < I(q = 0, \omega = \Omega)$. This result suggests that mobility effects are *enhanced* by the core-hole-lattice coupling. Setting $\lambda_{\text{CH}} = -1/2$, shown in Fig. 8c, results in more substantial changes; the phonon excitations nearly vanish because the local effective coupling $g_{\text{eff}} = 0$. However, there is a remnant at $q = \pi/a$, resulting from phonon excitation on neighboring sites.

When we increase the strength of the core-hole potential to $V_c = -12t$, the momentum dependence in the phonon excitation intensities is reduced, and spectra are more consistent with the predictions of the SS-LF model. For example, for $\lambda_{\text{CH}} = -1/2$, shown in Fig. 8f, the phonon excitations completely disappear, suggesting that the local effective coupling is zero and phonons are not being created on neighboring sites.

IV. SUMMARY & CONCLUSIONS

We have presented a detailed study of the XAS and RIXS spectra of a strongly correlated e -ph coupled system defined on an extended lattice. Using the DMRG method, we obtained numerically exact results while treating all aspects of the problem (electron kinetic energy, many-body interactions, and core-hole interactions) on an equal footing. We find that including electron mobility leads to additional \mathbf{q} -modulations in the phonon excitations, which is not present in the microscopic e -ph coupling constant. While the strength of these modulations appears to decrease with increasing U , they are still present deep in the Mott insulating regime.

Working on extended clusters has also allowed us to understand how many-body renormalizations and addi-

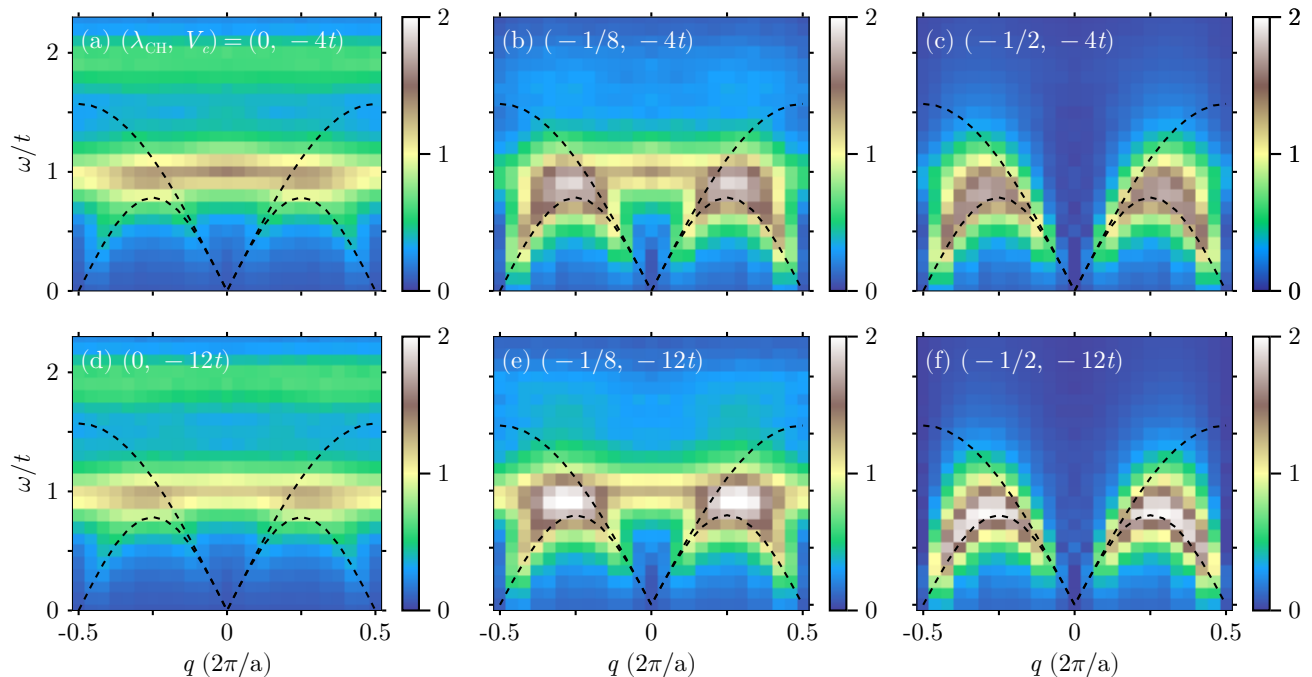


FIG. 8. RIXS spectra in the spin conserving channel as a function of the core-hole-lattice coupling and core-hole potential. The top row [panels (a) - (c)] shows results for $\lambda_{\text{CH}} = 0, -1/8,$ and $-1/2$ and weak core-hole potential $V_c = -4t$. The bottom row [panels (d) - (f)] shows similar results for $V_c = -12t$. The black dashed lines in all panels are the boundaries of the two-spinon continuum expected for the Hubbard model ($\lambda = 0$), assuming $J = 4t^2/U$. In all cases, we tuned the incident photon energies to the first peak in the XAS spectra, as indicated by the inverted triangles in Fig. 7. The RIXS results mostly follow the XAS resembling a local coupling $g_{\text{eff}} = g + g_{\text{CH}}$. However, the phonon intensities show highly nontrivial effects for $V_c = -4t$, especially in (c), where they are completely suppressed at the zone center but still visible at the zone boundary. All results were obtained on $L = 24$ site chains with fixed $\lambda = 1/2$, $U = 8t$, and $\Gamma/2 = t/4$.

tional core-hole-lattice interactions shape the resulting spectra. For example, CDW correlations appearing for smaller values of U significantly renormalized the phonon dispersion. The RIXS spectra reflect this renormalized dispersion, which lends support to the interpretation of several RIXS experiments where anomalous softening has been observed in proximity to CDW wave order [11, 15, 19]. Coupling between the lattice and the core hole was also found to modify the spectra in non-trivial ways, which will need to be accounted for.

Notably, the strength of many of these effects strongly depended on the magnitude of the core-hole potential; deep potentials tend to produce more localized intermediate states and bring our predictions more in line with the SS-LF model. Therefore, we expect these effects to be more pronounced at, for example, ligand K -edges than TM L -edges. Based on these observations, it may be possible to design an experimental protocol to contrast results obtained at different edges to unravel contributions from the intrinsic e -ph coupling, potential core-hole-lattice coupling, and electron delocalization.

Our results demonstrate that quantitative information about the e -ph coupling in correlated quantum materials cannot be directly obtained from data as implied by the SS-LF framework. For example, we believe that recent estimates [13, 14, 21] for the e -ph coupling extracted

from measurements of doped high- T_c cuprates are likely underestimated. Instead, this analysis will require detailed modeling, particularly when the core-hole potential is weak. Nevertheless, our DMRG framework sets the stage for a more detailed analysis of e -ph interactions in quasi-1D systems like the cuprate ladders and spin chains. Several experiments have already reported the observation of the Cu-O bond stretching phonons in these materials [6, 10, 53, 68]. A recent ARPES study of the doped cuprate $\text{Ba}_{2-x}\text{Sr}_x\text{CuO}_{3+\delta}$ [69] has inferred a sizable next-nearest-neighbor attraction that has been attributed to long-range e -ph coupling [70]. If true, this interaction should produce one or more phonon harmonics in the RIXS spectra, which can be simulated directly with our methods. These systems thus offer a unique opportunity for quantitative comparisons between theory and experiment. Finally, our work will stimulate future theoretical investigations of the e -ph coupling in time-resolved RIXS experiments, either using the Keldysh [71] or time-dependent scattering [72] approaches.

ACKNOWLEDGMENTS

We thank M. P. M. Dean and A. F. Kemper for valuable discussions. This work is supported by the National

Science Foundation under Grant No. DMR-1842056. A. N. acknowledges the support of the Canada First Research Excellence Fund. This work used computational resources and services provided by Advanced Research Computing at the University of British Columbia.

Appendix A: Lang-Firsov Limit

This section briefly reviews the single-site framework for analyzing RIXS data [2]. The starting point is the local Hamiltonian

$$\mathcal{H}_{\text{local}} = U\hat{n}_{\uparrow}\hat{n}_{\downarrow} + \Omega\hat{b}^{\dagger}\hat{b} + g\hat{n}(\hat{b}^{\dagger} + \hat{b}). \quad (\text{A1})$$

We have assumed that the localized electrons couple to dispersionless Einstein oscillators via a local coupling to the total density. In contrast, the derivation in Ref. [2] assumes a coupling to the change in electron density in the intermediate state, i.e. $H_{e\text{-ph}} = g\Delta n(b^{\dagger} + b)$, where $\Delta n = (n - \langle n \rangle)$ and $\langle n \rangle$ is the electron density in the ground state. The two forms for the e -ph interaction can be mapped to one another via a simple shift of the lattice equilibrium position in the atomic limit.

One can diagonalize Eq. (A1) by applying the canonical Lang-Firsov (LF) transformation $\mathcal{H}_{\text{LF}} = e^S \mathcal{H}_{\text{local}} e^{-S}$, where $S = \frac{g}{\Omega} \hat{n}(\hat{b}^{\dagger} - \hat{b})$, to obtain

$$\mathcal{H}_{\text{LF}} = U\hat{n}_{\uparrow}\hat{n}_{\downarrow} + \Omega\hat{b}^{\dagger}\hat{b} - \frac{g^2}{\Omega}\hat{n}^2. \quad (\text{A2})$$

Eq. (A2) must be supplemented with an additional core-hole term \mathcal{H}^{CH} when computing the intermediate states of the RIXS process, which results in a trivial shift of the eigenvalues $E_n \rightarrow E_n + 2V_c$.

The corresponding scattering amplitude to transition from the initial state i with zero phonons to the final state f with M phonons is given by [2]

$$F_{fi} = \sum_{M'=0}^{\infty} \frac{B_{\max(M,M'),\min(M,M')}(\frac{g}{\Omega}) B_{M',0}(\frac{g}{\Omega})}{\frac{4g^2}{\Omega} - M'\Omega - U - 2V_c + \omega_{\text{in}} + i\Gamma/2}. \quad (\text{A3})$$

Here, M' is the number of phonons in the intermediate state and

$$B_{M,M'}(x) = e^{-\frac{x^2}{2}} \sqrt{M!M'} \sum_{l=0}^{M'} \frac{(-1)^{M+l} x^{(2l+M-M')}}{(M'-l)! l! (M-M'+1)!}$$

is the Franck-Condon overlap factor. We obtain the total RIXS intensity by summing over final states using Eq. (2).

Appendix B: DMRG formalism for RIXS

Our approach is based on the Krylov space correction vector algorithm [38], which we briefly outline here. The first step is to expand the square of the matrix elements

in Eq. (3) to reformulate the problem using correction vectors [42, 73]

$$I(\mathbf{q}, \omega) \propto -\text{Im} \left[\sum_{j=1}^N \sum_{\sigma, \sigma', \gamma, \gamma'} e^{i\mathbf{q} \cdot (\mathbf{R}_j - \mathbf{R}_c)} \mathcal{I}_{j, \sigma, \sigma', \gamma, \gamma'} \right], \quad (\text{B1})$$

where

$$\mathcal{I}_{j, \sigma, \sigma', \gamma, \gamma'} = \langle \Psi_{j, \gamma} | D_{j, \gamma'} G D_{c, \sigma'}^{\dagger} | \Psi_{c, \sigma} \rangle \quad (\text{B2})$$

and

$$|\Psi_{j, \sigma}\rangle = \mathcal{G}_j D_{j, \sigma} |i\rangle. \quad (\text{B3})$$

Here, $|i\rangle$ is the ground state, σ, σ', γ , and γ' are spin indices, c denotes a site in the center of the cluster, and

$$\mathcal{G}_j = \frac{1}{E_i - \hat{\mathcal{H}}_j + \omega_{\text{in}} + i\Gamma/2}, \quad (\text{B4})$$

and

$$G = \frac{1}{E_i - \hat{\mathcal{H}} + \omega + i\eta} \quad (\text{B5})$$

are the electron Green's function with and without a core-hole, respectively. The intermediate state Hamiltonian \mathcal{H}_j in Eq. (B4) includes the interaction with the core-hole created at site j . The broadening parameter η in Eq. (B5) sets the resolution in energy loss ω and is typically set to the instrument broadening.

The XAS spectra are similarly formulated in the correction-vector method as

$$I_{\text{XAS}}(\omega_{\text{in}}) \propto -\text{Im} \langle i | D_{c, \sigma}^{\dagger} \mathcal{G}_c D_{c, \sigma} | i \rangle. \quad (\text{B6})$$

Appendix C: Dynamical correlation functions

In the main text, we show results for the dynamical charge structure factor and phonon spectral function, which are calculated using the correction vector method. The real-space charge correlation function is given by

$$N_{j,c}(\omega) = -\frac{1}{\pi} \text{Im} [\langle i | \tilde{n}_j G \tilde{n}_c | i \rangle]. \quad (\text{C1})$$

The phonon spectral function is given by

$$B_{j,c}(\omega) = -\frac{1}{\pi} \text{Im} [\langle i | \tilde{X}_j G \tilde{X}_c | i \rangle]. \quad (\text{C2})$$

Here, $|i\rangle$ is the ground state and $\tilde{n}_c = (\hat{n}_c - \langle \hat{n}_c \rangle)$ and $\tilde{X}_c = (\hat{X}_c - \langle \hat{X}_c \rangle)$, where c is the center site of the 1D chain. We then compute the momentum space dynamical correlation functions by Fourier transform [38].

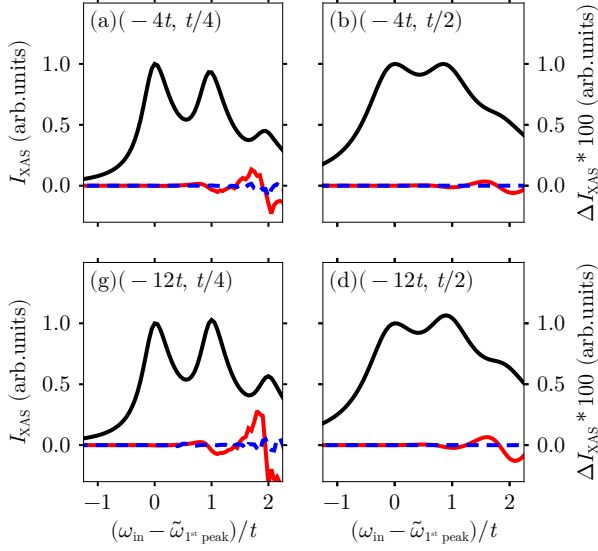


FIG. 9. Convergence tests of the XAS spectra obtained on an $L = 24$ site chain with $U = 8t$, $\lambda = 0.5$, $\lambda_{\text{CH}} = 0$. The solid black line is a reference XAS spectrum computed for different $(V_c, \Gamma/2)$ values as indicated in each panel. We kept a local phonon Hilbert space of $M = 16$ and $m = 500$ DMRG states for the reference case. The red (blue) lines show the difference of the XAS spectra calculated with $M = 17$, $m = 500$ ($M = 16$, $m = 600$), and the reference spectrum is shown in each panel.

Appendix D: Convergence tests

We have performed extensive convergence tests for our calculations. Here, we show representative results for a select few parameter regimes.

Figure 9 shows XAS spectra calculated on $L = 24$ site chains with $U = 8t$, $\lambda = 0.5$, $\lambda_{\text{CH}} = 0$ and different values of $(V_c, \Gamma/2)$, as indicated in each panel. Each panel shows a reference XAS spectrum computed after truncating the local phonon Hilbert space to $M = 16$ phonons per site and keeping $m = 500$ DMRG states. The red and blue lines show the difference between the reference spectrum and analogous XAS spectra calculated with $(M = 17, m = 500)$ and $(M = 16, m = 600)$, respectively. (Note that we have multiplied the difference curves by 100 to place them on a scale similar to the XAS spectra.) These results indicate that our spectra are well converged with respect to the size of the local phonon Hilbert space and the number of DMRG states.

Appendix E: Additional XAS results

Figure 10 plots additional XAS results for a strong core-hole potential $V_c = -12t$. We have fixed the core-hole lifetime to $\Gamma/2 = t/4$ and plotted results over a wider range of incident photon energies covering the PS resonance. The results indicate that only the WS resonance develops strong phonon satellites once the e -ph coupling is introduced.

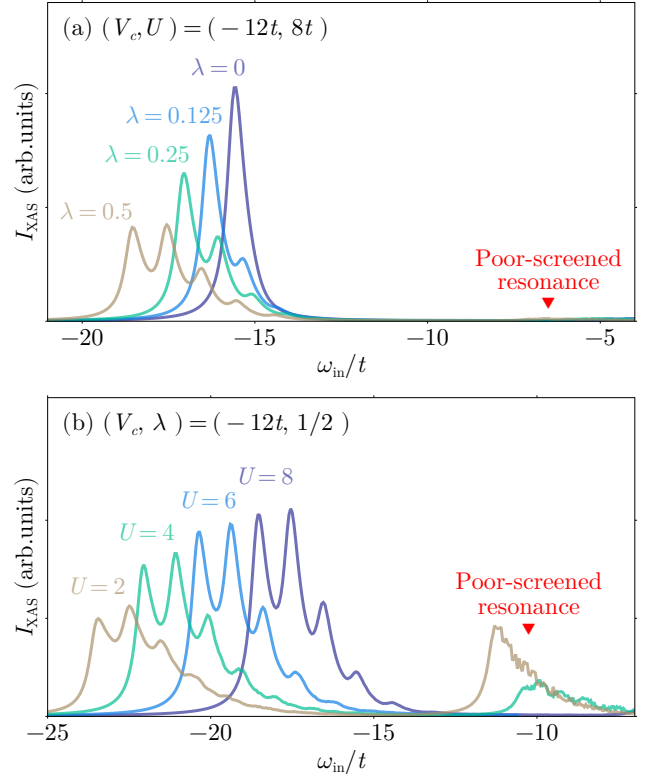


FIG. 10. Additional XAS results obtained for a strong core-hole potential $V_c = -12t$ and inverse core-hole lifetime $\Gamma/2 = t/4$. (a) The dependence of the XAS spectra as a function of the dimensionless e -ph coupling λ for a fixed $U = 8t$ and $\lambda_{\text{CH}} = 0$. (b) The dependence of the XAS spectra as a function of U for fixed $\lambda = 0.5$ and $\lambda_{\text{CH}} = 0$. The weight of the PS resonance is extremely small in the MI limit and is enhanced for smaller U values without generating any harmonics.

- [1] M. Mitrano, S. Johnston, Y.-J. Kim, and M. P. M. Dean, Exploring quantum materials with resonant inelastic x-ray scattering, *Phys. Rev. X* **14**, 040501 (2024).
 [2] L. J. P. Ament, M. van Veenendaal, and J. van den Brink, Determining the electron-phonon coupling strength from resonant inelastic x-ray scattering at transition metal L-

- edges, *EPL (Europhysics Letters)* **95**, 27008 (2011).
 [3] K. Gilmore, Quantifying vibronic coupling with resonant inelastic x-ray scattering, *Phys. Chem. Chem. Phys.* **25**, 217 (2023).
 [4] J. N. Hancock, G. Chabot-Couture, and M. Greven, Lattice coupling and Franck-Condon effects in K-edge res-

- onant inelastic x-ray scattering, *New Journal of Physics* **12**, 033001 (2010).
- [5] H. Yavaş, M. van Veenendaal, J. van den Brink, L. J. P. Ament, A. Alatas, B. M. Leu, M.-O. Apostu, N. Wizen, G. Behr, W. Sturhahn, H. Sinn, and E. E. Alp, Observation of phonons with resonant inelastic x-ray scattering, *Journal of Physics: Condensed Matter* **22**, 485601 (2010).
- [6] W. S. Lee, S. Johnston, B. Moritz, J. Lee, M. Yi, K. J. Zhou, T. Schmitt, L. Patthey, V. Strocov, K. Kudo, Y. Koike, J. van den Brink, T. P. Devereaux, and Z. X. Shen, Role of lattice coupling in establishing electronic and magnetic properties in quasi-one-dimensional cuprates, *Phys. Rev. Lett.* **110**, 265502 (2013).
- [7] J. J. Lee, B. Moritz, W. S. Lee, M. Yi, C. J. Jia, A. P. Sorini, K. Kudo, Y. Koike, K. J. Zhou, C. Monney, V. Strocov, L. Patthey, T. Schmitt, T. P. Devereaux, and Z. X. Shen, Charge-orbital-lattice coupling effects in the *dd* excitation profile of one-dimensional cuprates, *Phys. Rev. B* **89**, 041104 (2014).
- [8] S. Moser, S. Fatale, P. Krüger, H. Berger, P. Bugnon, A. Magrez, H. Niwa, J. Miyawaki, Y. Harada, and M. Griani, Electron-phonon coupling in the bulk of Anatase TiO₂ measured by resonant inelastic x-ray spectroscopy, *Phys. Rev. Lett.* **115**, 096404 (2015).
- [9] S. Fatale, S. Moser, J. Miyawaki, Y. Harada, and M. Griani, Hybridization and electron-phonon coupling in ferroelectric BaTiO₃ probed by resonant inelastic x-ray scattering, *Phys. Rev. B* **94**, 195131 (2016).
- [10] S. Johnston, C. Monney, V. Bisogni, K.-J. Zhou, R. Kraus, G. Behr, V. N. Strocov, J. Málek, S.-L. Drechsler, J. Geck, T. Schmitt, and J. van den Brink, Electron-lattice interactions strongly renormalize the charge-transfer energy in the spin-chain cuprate Li₂CuO₂, *Nature Communications* **7**, 10563 (2016).
- [11] L. Chaix, G. Ghiringhelli, Y. Y. Peng, M. Hashimoto, B. Moritz, K. Kummer, N. B. Brookes, Y. He, S. Chen, S. Ishida, Y. Yoshida, H. Eisaki, M. Salluzzo, L. Braicovich, Z. X. Shen, T. P. Devereaux, and W. S. Lee, Dispersive charge density wave excitations in Bi₂Sr₂CaCu₂O_{8+δ}, *Nature Physics* **13**, 952 (2017).
- [12] D. Meyers, K. Nakatsukasa, S. Mu, L. Hao, J. Yang, Y. Cao, G. Fabbris, H. Miao, J. Pellicciari, D. McNally, M. Dantz, E. Paris, E. Karapetrova, Y. Choi, D. Haskel, P. Shafer, E. Arenholz, T. Schmitt, T. Berlijn, S. Johnston, J. Liu, and M. P. M. Dean, Decoupling carrier concentration and electron-phonon coupling in oxide heterostructures observed with resonant inelastic x-ray scattering, *Phys. Rev. Lett.* **121**, 236802 (2018).
- [13] M. Rossi, R. Arpaia, R. Fumagalli, M. Moretti Sala, D. Betto, K. Kummer, G. M. De Luca, J. van den Brink, M. Salluzzo, N. B. Brookes, L. Braicovich, and G. Ghiringhelli, Experimental determination of momentum-resolved electron-phonon coupling, *Phys. Rev. Lett.* **123**, 027001 (2019).
- [14] L. Braicovich, M. Rossi, R. Fumagalli, Y. Peng, Y. Wang, R. Arpaia, D. Betto, G. M. De Luca, D. Di Castro, K. Kummer, M. Moretti Sala, M. Pagetti, G. Balestrino, N. B. Brookes, M. Salluzzo, S. Johnston, J. van den Brink, and G. Ghiringhelli, Determining the electron-phonon coupling in superconducting cuprates by resonant inelastic x-ray scattering: methods and results on Nd_{1+x}Ba_{2-x}Cu₃O_{7-δ}, *Phys. Rev. Research* **2**, 023231 (2020).
- [15] J. Li, A. Nag, J. Pellicciari, H. Robarts, A. Walters, M. Garcia-Fernandez, H. Eisaki, D. Song, H. Ding, S. Johnston, R. Comin, and K.-J. Zhou, Multiorbital charge-density wave excitations and concomitant phonon anomalies in Bi₂Sr₂LaCuO_{6+δ}, *Proceedings of the National Academy of Sciences* **117**, 16219 (2020).
- [16] J. Q. Lin, H. Miao, D. G. Mazzone, G. D. Gu, A. Nag, A. C. Walters, M. García-Fernández, A. Barbour, J. Pellicciari, I. Jarrige, M. Oda, K. Kurosawa, N. Momono, K.-J. Zhou, V. Bisogni, X. Liu, and M. P. M. Dean, Strongly correlated charge density wave in La_{2-x}Sr_xCuO₄ evidenced by doping-dependent phonon anomaly, *Phys. Rev. Lett.* **124**, 207005 (2020).
- [17] A. Geondzhian, A. Sambri, G. M. De Luca, R. Di Capua, E. Di Gennaro, D. Betto, M. Rossi, Y. Y. Peng, R. Fumagalli, N. B. Brookes, L. Braicovich, K. Gilmore, G. Ghiringhelli, and M. Salluzzo, Large polarons as key quasiparticles in SrTiO₃ and SrTiO₃-based heterostructures, *Phys. Rev. Lett.* **125**, 126401 (2020).
- [18] Y. Y. Peng, A. A. Husain, M. Mitranò, S. X.-L. Sun, T. A. Johnson, A. V. Zakrzewski, G. J. MacDougall, A. Barbour, I. Jarrige, V. Bisogni, and P. Abbamonte, Enhanced electron-phonon coupling for charge-density-wave formation in La_{1.8-x}Eu_{0.2}Sr_xCuO_{4+δ}, *Phys. Rev. Lett.* **125**, 097002 (2020).
- [19] H. Y. Huang, A. Singh, C. Y. Mou, S. Johnston, A. F. Kemper, J. van den Brink, P. J. Chen, T. K. Lee, J. Okamoto, Y. Y. Chu, J. H. Li, S. Komiya, A. C. Komarek, A. Fujimori, C. T. Chen, and D. J. Huang, Quantum fluctuations of charge order induce phonon softening in a superconducting cuprate, *Phys. Rev. X* **11**, 041038 (2021).
- [20] C. D. Dashwood, A. Geondzhian, J. G. Vale, A. C. Pakpour-Tabrizi, C. A. Howard, Q. Faure, L. S. I. Veiga, D. Meyers, S. G. Chiuzbăian, A. Nicolaou, N. Jaouen, R. B. Jackman, A. Nag, M. García-Fernández, K.-J. Zhou, A. C. Walters, K. Gilmore, D. F. McMorrow, and M. P. M. Dean, Probing electron-phonon interactions away from the Fermi level with resonant inelastic x-ray scattering, *Phys. Rev. X* **11**, 041052 (2021).
- [21] Y. Peng, L. Martinelli, Q. Li, M. Rossi, M. Mitranò, R. Arpaia, M. M. Sala, Q. Gao, X. Guo, G. M. De Luca, A. Walters, A. Nag, A. Barbour, G. Gu, J. Pellicciari, N. B. Brookes, P. Abbamonte, M. Salluzzo, X. Zhou, K.-J. Zhou, V. Bisogni, L. Braicovich, S. Johnston, and G. Ghiringhelli, Doping dependence of the electron-phonon coupling in two families of bilayer superconducting cuprates, *Phys. Rev. B* **105**, 115105 (2022).
- [22] M. Naamneh, E. Paris, D. McNally, Y. Tseng, W. R. Pudenko, D. J. Gawryluk, J. Shamblin, E. OQuinn, B. Cohen-Stead, M. Shi, M. Radovic, M. Lang, T. Schmitt, S. Johnston, and N. C. Plumb, Persistence of small polarons into the superconducting phase of Ba_{1-x}K_xBiO₃, [arXiv:2408.00401](https://arxiv.org/abs/2408.00401) (2024).
- [23] T. P. Devereaux, A. M. Shvaika, K. Wu, K. Wohlfeld, C. J. Jia, Y. Wang, B. Moritz, L. Chaix, W.-S. Lee, Z.-X. Shen, G. Ghiringhelli, and L. Braicovich, Directly characterizing the relative strength and momentum dependence of electron-phonon coupling using resonant inelastic x-ray scattering, *Phys. Rev. X* **6**, 041019 (2016).
- [24] A. Geondzhian and K. Gilmore, Generalization of the Franck-Condon model for phonon excitations by resonant inelastic x-ray scattering, *Phys. Rev. B* **101**, 214307 (2020).

- [25] K. Bieniasz, S. Johnston, and M. Berciu, Beyond the single-site approximation modeling of electron-phonon coupling effects on resonant inelastic X-ray scattering spectra, *SciPost Phys.* **11**, 62 (2021).
- [26] K. Bieniasz, S. Johnston, and M. Berciu, Theory of dispersive optical phonons in resonant inelastic x-ray scattering experiments, *Phys. Rev. B* **105**, L180302 (2022).
- [27] A. Geondzhian and K. Gilmore, Demonstration of resonant inelastic x-ray scattering as a probe of exciton-phonon coupling, *Phys. Rev. B* **98**, 214305 (2018).
- [28] A. Nocera, U. Kumar, N. Kaushal, G. Alvarez, E. Dagotto, and S. Johnston, Computing resonant inelastic x-ray scattering spectra using the density matrix renormalization group method, *Scientific Reports* **8**, 11080 (2018).
- [29] S. Karakuzu, L. F. Tocchio, S. Sorella, and F. Becca, Superconductivity, charge-density waves, antiferromagnetism, and phase separation in the Hubbard-Holstein model, *Phys. Rev. B* **96**, 205145 (2017).
- [30] N. C. Costa, K. Seki, S. Yunoki, and S. Sorella, Phase diagram of the two-dimensional Hubbard-Holstein model, *Communications Physics* **3**, 80 (2020).
- [31] R. P. Hardikar and R. T. Clay, Phase diagram of the one-dimensional Hubbard-Holstein model at half and quarter filling, *Phys. Rev. B* **75**, 245103 (2007).
- [32] M. Tezuka, R. Arita, and H. Aoki, Phase diagram for the one-dimensional Hubbard-Holstein model: a density-matrix renormalization group study, *Phys. Rev. B* **76**, 155114 (2007).
- [33] M. Hohenadler and H. Fehske, Density waves in strongly correlated quantum chains, *The European Physical Journal B* **91**, 204 (2018).
- [34] L. Braicovich, L. J. P. Ament, V. Bisogni, F. Forte, C. Aruta, G. Balestrino, N. B. Brookes, G. M. De Luca, P. G. Medaglia, F. M. Granozio, M. Radovic, M. Salluzzo, J. van den Brink, and G. Ghiringhelli, Dispersion of magnetic excitations in the cuprate La_2CuO_4 and CaCuO_2 compounds measured using resonant x-ray scattering, *Phys. Rev. Lett.* **102**, 167401 (2009).
- [35] V. Bisogni, S. Kourtis, C. Monney, K. Zhou, R. Kraus, C. Sekar, V. Strocov, B. Büchner, J. van den Brink, L. Braicovich, T. Schmitt, M. Daghofer, and J. Geck, Femtosecond dynamics of momentum-dependent magnetic excitations from resonant inelastic x-ray scattering in CaCu_2O_3 , *Phys. Rev. Lett.* **112**, 147401 (2014).
- [36] S. R. White, Density matrix formulation for quantum renormalization groups, *Physical Review Letters* **69**, 2863–2866 (1992).
- [37] S. R. White, Density-matrix algorithms for quantum renormalization groups, *Physical Review B* **48**, 10345–10356 (1993).
- [38] A. Nocera and G. Alvarez, Spectral functions with the density matrix renormalization group: Krylov-space approach for correction vectors, *Physical Review E* **94**, 053308 (2016).
- [39] Y. Lu and M. W. Haverkort, Nonperturbative series expansion of Green's functions: the anatomy of resonant inelastic x-ray scattering in the doped Hubbard model, *Phys. Rev. Lett.* **119**, 256401 (2017).
- [40] J. van den Brink and M. van Veenendaal, Correlation functions measured by indirect resonant inelastic x-ray scattering, *Europhys. Lett.* **73**, 121 (2005).
- [41] A. M. Tsvelik, R. M. Konik, N. V. Prokof'ev, and I. S. Tupitsyn, Resonant inelastic x-ray scattering in metals: a diagrammatic approach, *Phys. Rev. Research* **1**, 033093 (2019).
- [42] T. D. Kühner and S. R. White, Dynamical correlation functions using the density matrix renormalization group, *Phys. Rev. B* **60**, 335 (1999).
- [43] S. R. White and A. E. Feiguin, Real-time evolution using the density matrix renormalization group, *Phys. Rev. Lett.* **93**, 076401 (2004).
- [44] G. Alvarez, The density matrix renormalization group for strongly correlated electron systems: a generic implementation, *Computer Physics Communications* **180**, 1572 (2009).
- [45] S. Kourtis, J. van den Brink, and M. Daghofer, Exact diagonalization results for resonant inelastic x-ray scattering spectra of one-dimensional mott insulators, *Phys. Rev. B* **85**, 064423 (2012).
- [46] K. Tsutsui, T. Tohyama, and S. Maekawa, Resonant inelastic x-ray scattering in one-dimensional copper oxides, *Physical Review B* **61**, 7180–7182 (2000).
- [47] T. Giamarchi, *Quantum Physics in One Dimension* (Oxford University Press, 2003).
- [48] D. A. Tennant, R. A. Cowley, S. E. Nagler, and A. M. Tsvelik, Measurement of the spin-excitation continuum in one-dimensional KCuF_3 using neutron scattering, *Phys. Rev. B* **52**, 13368 (1995).
- [49] I. A. Zaliznyak, C. Broholm, M. Kibune, M. Nohara, and H. Takagi, Anisotropic spin freezing in the $S = 1/2$ zigzag chain compound SrCuO_2 , *Phys. Rev. Lett.* **83**, 5370 (1999).
- [50] A. C. Walters, T. G. Perring, J.-S. Caux, A. T. Savici, G. D. Gu, C.-C. Lee, W. Ku, and I. A. Zaliznyak, Effect of covalent bonding on magnetism and the missing neutron intensity in copper oxide compounds, *Nature Physics* **5**, 867 (2009).
- [51] M. Mourigal, M. Enderle, A. Klöpperpieper, J.-S. Caux, A. Stunault, and H. M. Rønnow, Fractional spinon excitations in the quantum Heisenberg antiferromagnetic chain, *Nature Physics* **9**, 435 (2013).
- [52] J. Schlappa, K. Wohlfeld, K. J. Zhou, M. Mourigal, M. W. Haverkort, V. N. Strocov, L. Hozoi, C. Monney, S. Nishimoto, S. Singh, A. Revcolevschi, J. S. Caux, L. Patthey, H. M. Rønnow, J. van den Brink, and T. Schmitt, Spin-orbital separation in the quasi-one-dimensional Mott insulator Sr_2CuO_3 , *Nature* **485**, 82 (2012).
- [53] J. Schlappa, U. Kumar, K. J. Zhou, S. Singh, M. Mourigal, V. N. Strocov, A. Revcolevschi, L. Patthey, H. M. Rønnow, S. Johnston, and T. Schmitt, Probing multi-spinon excitations outside of the two-spinon continuum in the antiferromagnetic spin chain cuprate Sr_2CuO_3 , *Nature Communications* **9**, 5394 (2018).
- [54] U. Kumar, A. Nag, J. Li, H. C. Robarts, A. C. Walters, M. García-Fernández, R. Saint-Martin, A. Revcolevschi, J. Schlappa, T. Schmitt, S. Johnston, and K.-J. Zhou, Unraveling higher-order contributions to spin excitations probed using resonant inelastic x-ray scattering, *Phys. Rev. B* **106**, L060406 (2022).
- [55] B. J. Kim, H. Koh, E. Rotenberg, S. J. Oh, H. Eisaki, N. Motoyama, S. Uchida, T. Tohyama, S. Maekawa, Z. X. Shen, and C. Kim, Distinct spinon and holon dispersions in photoemission spectral functions from one-dimensional SrCuO_2 , *Nature Physics* **2**, 397 (2006).
- [56] U. Kumar, A. Nocera, E. Dagotto, and S. Johnston, Multi-spinon and antiholon excitations probed by reso-

- nant inelastic x-ray scattering on doped one-dimensional antiferromagnets, *New Journal of Physics* **20**, 073019 (2018).
- [57] S. Li, A. Nocera, U. Kumar, and S. Johnston, Particle-hole asymmetry in the dynamical spin and charge responses of corner-shared 1D cuprates, *Communications Physics* **4**, 217 (2021).
- [58] L. J. P. Ament, G. Ghiringhelli, M. M. Sala, L. Braicovich, and J. van den Brink, Theoretical demonstration of how the dispersion of magnetic excitations in cuprate compounds can be determined using resonant inelastic x-ray scattering, *Phys. Rev. Lett.* **103**, 117003 (2009).
- [59] M. J. Bhaseen, F. H. L. Essler, and A. Grage, Itinerancy effects on spin correlations in one-dimensional Mott insulators, *Physical Review B* **71**, 020405 (2005).
- [60] A. Klauser, J. Mossel, J.-S. Caux, and J. Van Den Brink, Spin-Exchange Dynamical Structure Factor of the $S = 1/2$ Heisenberg chain, *Physical Review Letters* **106**, 157205 (2011).
- [61] C. Jia, K. Wohlfeld, Y. Wang, B. Moritz, and T. P. Devereaux, Using RIXS to uncover elementary charge and spin excitations, *Phys. Rev. X* **6**, 021020 (2016).
- [62] F. Forte, M. Cuoco, C. Noce, and J. van den Brink, Doping dependence of magnetic excitations of one-dimensional cuprates as probed by resonant inelastic x-ray scattering, *Phys. Rev. B* **83**, 245133 (2011).
- [63] A. Scheie, P. Laurell, A. M. Samarakoon, B. Lake, S. E. Nagler, G. E. Granroth, S. Okamoto, G. Alvarez, and D. A. Tennant, Witnessing entanglement in quantum magnets using neutron scattering, *Phys. Rev. B* **103**, 224434 (2021).
- [64] P. Laurell, A. Scheie, E. Dagotto, and D. A. Tennant, Witnessing entanglement and quantum correlations in condensed matter: a review, [arXiv:2405.10899](https://arxiv.org/abs/2405.10899) (2024).
- [65] T. Ren, Y. Shen, S. F. R. TenHuisen, J. Sears, W. He, M. H. Upton, D. Casa, P. Becker, M. Mitranò, M. P. M. Dean, and R. M. Konik, Witnessing quantum entanglement using resonant inelastic x-ray scattering, [arXiv:2404.05850](https://arxiv.org/abs/2404.05850) (2024).
- [66] M. Weber, F. F. Assaad, and M. Hohenadler, Phonon spectral function of the one-dimensional Holstein-Hubbard model, *Phys. Rev. B* **91**, 235150 (2015).
- [67] S. Johnston, F. Vernay, B. Moritz, Z.-X. Shen, N. Nagaosa, J. Zaanen, and T. P. Devereaux, Systematic study of electron-phonon coupling to oxygen modes across the cuprates, *Phys. Rev. B* **82**, 064513 (2010).
- [68] Y. Tseng, J. Thomas, W. Zhang, E. Paris, P. Pupal, R. Bag, G. Deng, T. C. Asmara, V. N. Strocov, S. Singh, E. Pomjakushina, U. Kumar, A. Nocera, H. M. Rønnow, S. Johnston, and T. Schmitt, Crossover of high-energy spin fluctuations from collective triplons to localized magnetic excitations in $\text{Sr}_{14-x}\text{Ca}_x\text{Cu}_{24}\text{O}_{41}$ ladders, *npj Quantum Materials* **7**, 92 (2022).
- [69] Z. Chen, Y. Wang, S. N. Rebec, T. Jia, M. Hashimoto, D. Lu, B. Moritz, R. G. Moore, T. P. Devereaux, and Z.-X. Shen, Anomalously strong near-neighbor attraction in doped 1D cuprate chains, *Science* **373**, 1235 (2021).
- [70] Y. Wang, Z. Chen, T. Shi, B. Moritz, Z.-X. Shen, and T. P. Devereaux, Phonon-mediated long-range attractive interaction in one-dimensional cuprates, *Phys. Rev. Lett.* **127**, 197003 (2021).
- [71] Y. Chen, Y. Wang, C. Jia, B. Moritz, A. M. Shvaika, J. K. Freericks, and T. P. Devereaux, Theory for time-resolved resonant inelastic x-ray scattering, *Phys. Rev. B* **99**, 104306 (2019).
- [72] K. Zawadzki, A. Nocera, and A. E. Feiguin, A time-dependent momentum-resolved scattering approach to core-level spectroscopies, *SciPost Phys.* **15**, 166 (2023).
- [73] E. Jeckelmann, Dynamical density-matrix renormalization-group method, *Phys. Rev. B* **66**, 045114 (2002).